43rd AIAA Aerospace Sciences Meeting and Exhibit
Jan 10–13, 2005/Reno, Nevada AIAA 2005-0833

Prediction of Flutter and LCO by an Euler Method on Non-moving Cartesian Grids with Boundary-Layer Corrections

Zhichao Zhang*, Shuchi Yang† and Feng Liu‡
Department of Mechanical and Aerospace Engineering
University of California, Irvine, CA 92697-3975

David M. Schuster§
Aeroelasticity Branch
NASA Langley Research Center, Hampton, VA 23681

We present an unsteady Euler method on non-moving cartesian grids coupled with an integral boundary-layer method for the prediction of flutter. The Isogai 2-D wing model are computed by 5 methods: (1) Euler method on the non-moving cartesian grid without the boundary-layer correction; (2) Euler method on body-fitted moving grids without the boundary-layer correction; (3) Euler method on the non-moving cartesian grid coupled with the integral boundary-layer method; (4) Euler method on body-fitted moving grids coupled with the integral boundary-layer method; (5) Full Navier-Stokes method on body-fitted moving grids. Comparisons will be made of the computed flutter boundary and frequency as well as LCO magnitude versus speed index at various transonic Mach numbers. The effect of viscosity and the applicability of the Euler method on non-moving cartesian grids with approximate boundary conditions are assessed.

I. Introduction

Computational Fluid Dynamics (CFD) has proven to be a useful tool for the simulation and prediction of many unsteady phenomena of aeroelastic systems such as buffet, flutter, and Limit Cycle Oscillation (LCO). Methods ranging from the linear doublet-lattice method[1] to methods that solve the Euler and the Navier-Stokes equations have been developed.[2–7] Despite its limit in handling transonic and other nonlinear flows, the linear doublet-lattice method has been and is still the workhorse for actual design analysis in industry because of its efficiency in computer time and, perhaps equally important, the ease in setting up the computational problem. The Reynolds-Averaged-Navier-Stokes (RANS) methods encompass the most complete flow model short of Large-Eddy-Simulations (LES) or Direct-Numerical-Simulations (DNS). However, RANS simulations for aeroelasticity problems at present demand undesirably large amounts of computational resources in a design environment. In addition, their usefulness is hampered by uncertainties in turbulence modeling, grid resolution, and numerical damping effects;[6,7] difficulties in grid generation and the transfer of displacements and aerodynamic forces between the structural and aerodynamic grids; and lack of fast and robust algorithms for deforming grids needed in the unsteady computations. In between the above two extremes, methods based on the various forms of the potential flow equation with boundary-layer corrections have shown good results for unsteady calculation without the use of large computational resources and with less human work in setting up the computational problem including grid generation. Among such methods, the CAP-TSD[8–10] code is widely known and used. The CAP-TSD code has many advantages over

*Graduate student. AIAA member.
†Post-doctoral researcher. AIAA member.
‡Professor. Associate Fellow AIAA.
§Senior Research Engineer. Associate Fellow AIAA.

a full-fledged RANS code. These include 1) ease in generating a grid; 2) no need to do complex interpolation between the structural and CFD grids; 3) no need to have a moving grid; 4) less demand on CPU time and memory.

Despite the use of vortex and entropy corrections, the potential flow assumption in CAP-TSD limits its applicability to irrotational flows with weak shocks. On the other hand, Euler methods are capable of resolving strong shocks and transporting vortices correctly, and advances in computer speed and maturity of algorithms for the Euler equations have made the solution of the Euler equations a rather dependable and routine tool. Due to the requirement of large computing resources by a Navier-Stokes code and also unresolved issues regarding accuracy of current numerical algorithms for the Navier-Stokes equations, the Euler method with boundary layer coupling provides a good balance between completeness of the flow model and computational efficiency. In fact, interactive boundary-layer methods using the Euler equations have been investigated by many researchers.[11–14] However, most of them focus on steady calculations.

In order to use the Euler equations but retain the ease in setting up a computational grid as in the CAPTSD code, References 15 and 16 develop an unsteady Euler solver for aeroelastic applications on stationary Cartesian grids through the use of approximate boundary conditions. The full Euler boundary conditions on the airfoil surface are replaced by their first-order expansions on the mean chord line of the airfoil for thin airfoils with small deformations, which is usually the case for flutter predictions for moving or deforming airfoils. Although the thickness of the airfoil and the unsteady deformation from the mean positions are required to be small because of the use of the approximate boundary conditions, the mean angle of attack is not formally under the same small perturbation restriction. By using these approximate boundary conditions, we can avoid the use of a body-fitted moving or deforming grid, which can be a rather time-consuming and non-trivial task for practical problems.[17] Details of the mathematical formulation of the approximate boundary conditions and validation of the code for both steady, unsteady, and aeroelastic calculations are presented in Refs. 15 and 16, where the method is shown to provide excellent results for flutter predictions and be able to predict LCO for the two-dimensional Isogai wing model. Dowell et al.[18] present a latest review on nonlinear aeroelasticity, in which they cited spread of computational data on the prediction of the flutter boundary and LCO amplitude for the two-dimensional Isogai wing model[19,20] by different computational methods ranging from the transonic-small-disturbance method to full Navier-Stokes methods. They also pointed out the importance of including viscous effects on LCO amplitude. In this work, we extend the work in Refs. 15 and 16 to include an integral boundary layer method to account for viscous effects. We use the Isogai wing model as a benchmark test case to compare the following five methods for the prediction of the flutter boundary and LCO for a few typical transonic flight Mach numbers.

1. Euler method on the non-moving cartesian grid without the boundary-layer correction;
2. Euler method on body-fitted moving grids without the boundary-layer correction;
3. Euler method on the non-moving cartesian grid coupled with the integral boundary-layer method;
4. Euler method on body-fitted moving grids coupled with the integral boundary-layer method;
5. Full Navier-Stokes method on body-fitted moving grids.

Through this detailed systematic study, we hope to clarify the validity of the various assumptions in the prediction of the two typical aeroelastic phenomena and the applicability of the numerical methods.

II. Numerical Method

The five methods listed above have already been developed and validated.[4,16,21–23] For convenience, here we briefly describe the basics including unsteady Euler method, the approximate boundary condition approach on non-moving cartesian grids, the integral boundary layer method and its coupling with the Euler solver, the full Navier-Stokes method using $k-\omega$ turbulence model, and the structural solver as well as the strong coupling CFD-CSD scheme.

A. Time-Accurate Euler Method

The two-dimensional unsteady Euler equations in conservative integral form over a fixed control volume V enclosed by the surface S are:

$$\frac{\partial}{\partial t}\int_V \mathbf{W}dV + \int_S \mathbf{G}\cdot\mathbf{n}dS = 0 \tag{1}$$

where

$$\mathbf{W} = \begin{bmatrix} \rho \\ \rho u \\ \rho v \\ \rho E \end{bmatrix} \tag{2}$$

$$\mathbf{G} = \begin{bmatrix} \rho\mathbf{q} \\ \rho u\mathbf{q} + p\mathbf{e}_x \\ \rho v\mathbf{q} + p\mathbf{e}_y \\ \rho E\mathbf{q} + p(u\mathbf{e}_x + v\mathbf{e}_y) \end{bmatrix} \tag{3}$$

$$\mathbf{q} = u\mathbf{e}_x + v\mathbf{e}_y \tag{4}$$

$$E = \frac{1}{\gamma - 1}\frac{p}{\rho} + \frac{1}{2}(u^2 + v^2) \tag{5}$$

Applying (1) to each cell in the mesh we obtain a set of ordinary differential equations of the form

$$\frac{d}{dt}(\mathbf{W}_{i,j}V_{i,j}) + \mathbf{R}(\mathbf{W}_{i,j}) = 0 \tag{6}$$

where $V_{i,j}$ is the volume of the i,j cell and the residual $\mathbf{R}(\mathbf{W}_{i,j})$ is obtained by evaluating the flux integral in (1). Following Jameson,[24] we approximate the $\frac{d}{dt}$ operator by an implicit backward difference formula of second-order accuracy in the following form (dropping the subscripts i,j for clarity)

$$\frac{3}{2\Delta t}[\mathbf{W}^{n+1}V] - \frac{2}{\Delta t}[\mathbf{W}^{n}V] + \frac{1}{2\Delta t}[\mathbf{W}^{n-1}V] + \mathbf{R}(\mathbf{W}^{n+1}) = 0 \tag{7}$$

Eqn. (7) can be solved for $\mathbf{W}^{n+1}$ at each time step by solving the following steady-state problem in a pseudo time t^*.

$$\frac{d\mathbf{W}}{dt^*} + \mathbf{R}^*(\mathbf{W}) = 0 \tag{8}$$

where

$$\mathbf{R}^*(\mathbf{W}) = \mathbf{R}(\mathbf{W}) + \frac{3}{2\Delta t}(\mathbf{W}V) - \frac{2}{\Delta t}(\mathbf{W}^{n}V) + \frac{1}{2\Delta t}(\mathbf{W}^{n-1}V) \tag{9}$$

Eqn.(8) is solved by an explicit time-marching scheme in t^* for which the local time stepping, residual smoothing, and multigrid techniques[25] can be used to accelerate convergence to a steady state solution.

B. Approximate Boundary Conditions on Non-moving Cartesian Grids

Gao et al.[15] applied the above time-accurate Euler scheme on stationary Cartesian grids for unsteady calculations using a small-perturbation boundary condition treatment.

A thin airfoil slightly moving or deforming about its mean position is considered. For the flutter calculation in the present paper, the airfoil is assumed to be of rigid shape but performs pitching or plunging motion. The mean position of the airfoil chord lies on the horizontal axis x of the coordinate system between

$x = 0$ and $x = 1$. The velocity of the incoming uniform free stream makes an angle α_m with the x axis. The shape of the airfoil is described by $y = f(x)$ and $g(x)$ for its upper and lower surfaces, respectively. The instantaneous position of the airfoil is described by $y = F(t, x)$ and $y = G(t, x)$ for the upper and lower surfaces, respectively. Under the assumption, $|F| \ll 1$, the first-order approximation of the boundary conditions on the upper surface of the airfoil at an instant t is

$$v(t, x, 0) = u(t, x, 0)F_x + F_t + O(F) \tag{10}$$

where the subscripts, x and t denote the partial derivatives with respect to x and t, respectively; $O(F)$ represents terms of the same order of magnitude as F or higher. The normal velocity boundary condition on the lower surface is treated similarly.

There are altogether four independent variables in the Euler equations (1), e.g. ρ, u, v and p. In addition to the boundary condition for the normal velocity v given above, three more conditions are needed on the airfoil surfaces. Among them, ρ and u can be simply extrapolated from the first several cells adjacent to the wall, whereas p need to be calculated using the normal momentum equation. The momentum differential equation in the outward normal direction $\mathbf{n}$ is

$$\mathbf{n} \cdot [\frac{\partial \mathbf{q}}{\partial t} + (\mathbf{q} \cdot \nabla)\mathbf{q}] = \mathbf{n} \cdot (-\frac{\nabla p}{\rho}) \tag{11}$$

On the upper surface of the airfoil, $y = F(t, x)$, the above equation becomes

$$p_y(t, x, F) = F_x p_x(t, x, F) - \rho(t, x, F)[F_{tt} + 2F_{tx}u(t, x, F) + F_{xx}u^2(t, x, F)] \tag{12}$$

The first-order approximation of the above equation is

$$p_y(t, x, 0) = F_x p_x(t, x, 0) - \rho(t, x, 0)[F_{tt} + 2F_{tx}u(t, x, 0) + F_{xx}u^2(t, x, 0)] + O(F) \tag{13}$$

The corresponding equations on the lower surface of the airfoil are similarly derived.

For airfoil pitching, the instantaneous angle from the mean position is $\alpha_1(t)$, positive in clockwise direction. Given $f(x)$, the instantaneous ordinate of the upper surface, $F(t, x)$, is expressed implicitly as follows.

$$F \cos\alpha_1 + (x - x_0)\sin\alpha_1 = f\left(x_0 + (x - x_0)\cos\alpha_1 - F\sin\alpha_1\right) \tag{14}$$

where the expression $x_0 + (x - x_0)\cos\alpha_1 - F\sin\alpha_1$ in the first pair of parentheses on the right-hand-side of the equation is the argument of the function $f(x)$.

The five derivatives of $F(t, x)$ used in Eqn. (13) can be evaluated approximately as following:

$$\begin{aligned}
F_x &= f' - \tan\alpha_1 + O(F^3) \\
F_{xx} &= f'' + O(F^3) \\
F_t &= -\alpha_1'(x - x_0)\sec^2\alpha_1 + O(F^3) \\
F_{tx} &= -\alpha_1'\sec^2\alpha_1 + O(F^3) \\
F_{tt} &= -(x - x_0)\sec^2\alpha_1(\alpha_1'' + 2\alpha_1'^2\tan\alpha_1) + O(F^3)
\end{aligned} \tag{15}$$

where the $'$ denotes differentiation of $f(x)$ and $\alpha(t)$ with respect to x and t, respectively.

C. Interactive Boundary-Layer Method

On consideration of computational cost as well as uncertainties of turbulence modeling involved in a finite difference method, we use an integral boundary-layer method to account for the viscous effect. The classical boundary-layer calculation is to solve the boundary-layer thickness using the boundary-layer edge pressure gradient obtained from the outer inviscid flow solver. However, it is well known that this so-called direct method of boundary-layer calculation breaks down for flows involving strong inviscid-viscous interactions, especially when separation exists. Thus we couple the inverse boundary-layer calculation with the outer inviscid flow solution. In an inverse boundary-layer calculation, on the other hand, the edge pressure or

velocity is solved from a given distribution of boundary-layer displacement thickness. More conveniently, following Cater[26] , we introduce the perturbation mass flow parameter $\overline{m} = \rho_e U_e \delta^*$. For a given distribution of $\overline{m}$ along the wall, we solve the boundary-layer edge velocity U_e.

By definition, $\delta^* = H\theta$, so expanding $\frac{d\overline{m}}{ds} = \frac{d(\rho_e U_e H\theta)}{ds}$ we get:

$$\frac{1}{\overline{m}}\frac{d\overline{m}}{ds} = \frac{1}{H}\frac{dH}{ds} + \frac{1}{\theta}\frac{d\theta}{ds} + (1 - M_e^2)\frac{1}{U_e}\frac{dU_e}{ds} \tag{16}$$

where δ and θ are the boundary-layer displacement and momentum thicknesses; ρ_e, U_e and M_e are local air density, velocity and Mach number at the boundary-layer edge, respectively; s is the streamwise coordinate along the airfoil wall or wake; H is the boundary-layer shape factor.

Considering the correlation between the shape factor H and the kinematic shape factor $\overline{H}$, i.e. $H = R_1(\overline{H} + 1) - 1$, we have:

$$\frac{dH}{ds} = R_1\frac{d\overline{H}}{ds} + (H + 1)\frac{R_3}{U_e}\frac{dU_e}{ds} \tag{17}$$

Thus eqn. (16) becomes:

$$\frac{H\theta}{\overline{m}}\frac{d\overline{m}}{ds} = H\frac{d\theta}{ds} + R_1\theta\frac{d\overline{H}}{ds} + [(H + 1)R_3 + H(1 - M_e^2)]\frac{\theta}{U_e}\frac{dU_e}{ds} \tag{18}$$

Here, R_1, R_2 , and R_3 are three parameters defined for convenience which are related to the ratio of specific heats γ, temperature recovery factor r, and the local boundary-layer edge Mach number M_e :

$$\begin{aligned} R_1 &= 1 + \frac{\gamma - 1}{2} r M_e^2 \\ R_2 &= 1 + \frac{\gamma - 1}{2} M_e^2 \\ R_3 &= \frac{(\gamma - 1) r M_e^2 R_2}{R_1} \end{aligned} \tag{19}$$

For a turbulent boundary-layer , Head[27] introduced the entrainment coefficient C_E, which stands for the rate at which fluid from the outer inviscid flow enters the boundary-layer through the boundary-layer edge. By definition,

$$C_E = \frac{1}{\rho_e U_e}\frac{d(\rho_e U_e H_1 \theta)}{ds} \tag{20}$$

where H_1 is Head's shape factor. Again, expanding the derivative we get:

$$C_E = H_1\frac{d\theta}{ds} + H_1(1 - M_e^2)\frac{\theta}{U_e}\frac{dU_e}{ds} + \theta\frac{dH_1}{d\overline{H}}\frac{d\overline{H}}{ds} \tag{21}$$

In addition, we have the integral momentum equation for compressible boundary-layer:

$$\frac{C_f}{2} = \frac{d\theta}{ds} + (H + 2 - M_e^2)\frac{\theta}{U_e}\frac{dU_e}{ds} \tag{22}$$

Thus we obtain a linear system of equations (18),(21), and (22) about three unknown derivatives : $\frac{d\theta}{ds}$, $\frac{dU_e}{ds}$, and $\frac{d\overline{H}}{ds}$. Solving it, we have now a system of three first-order ordinary differential equations about three boundary-layer parameters: θ, U_e, and $\overline{H}$.

In addition, we employ Green's lag equation[28] to account for the history effects in nonequilibrium turbulent boundary-layer:

$$\begin{aligned} \theta\frac{dC_E}{ds} &= \overline{F}\left\{\frac{2.8}{H + H_1}\left[(C_\tau)_{EQ0}^{0.5} - \lambda(C_\tau)^{0.5}\right]\right. \\ &\quad \left. - \left[1 + 0.075M_e^2\frac{R_1}{1 + 0.1M_e^2}\right]\frac{\theta}{U_e}\frac{dU_e}{ds} + \left(\frac{\theta}{U_e}\frac{dU_e}{ds}\right)_{EQ}\right\} \end{aligned} \tag{23}$$

Here, C_τ is the shear stress coefficient, λ is a parameter to account for secondary effects, $\overline{F}$ is another parameter to be defined in the Appendix. The subscript EQ denotes quantities evaluated under equilibrium conditions where the shape factor and the entrainment coefficient are invariant, while $EQ0$ denotes quantities evaluated under equilibrium flow free of secondary effects.

Therefore, totally we have a system of four first-order ordinary differential equations for the four unknown boundary-layer parameters . Given a distribution of $\overline{m}$ along the wall plus the initial values at a starting point such as a fixed transition point, we can integrate the four ordinary differential equations using Runge-Kutta method and solve for the four unknown boundary-layer parameters: θ, U_e, $\overline{H}$, and C_E. As for correlations of various parameters in the four equations, i.e. C_f, F, H_1, C_τ, $(\frac{\theta}{U_e}\frac{dU_e}{ds})_{EQ}$, and $(C_\tau)^{0.5}_{EQ0}$, etc., we follow those in Green's paper[28] . For completeness, we list them in the Appendix.

Given the boundary-layer edge properties obtained from the outer inviscid solver, we can use Thwaites' method[29] to calculate the laminar part of the boundary-layer starting from the stagnation point. Transition is either specified or determined using Michel's formula[30] :

$$Re_\theta > 1.174(1 + \frac{22400}{Re_s})Re_s^{0.46} \tag{24}$$

For the turbulent part, the boundary-layer calculation needs to be coupled with the outer Equivalent Inviscid Flow(EIF) calculation. We employ Carter's "semi-inverse" coupling scheme[31] . We first guess a distribution of the boundary-layer displacement thickness δ^*. Using ρ_e and U_e from a preliminary inviscid calculation, we obtain a guessed perturbation mass-flow parameter $\overline{m} = \rho_e U_e \delta^*$. An inverse boundary-layer calculation following the last section gives us a viscous version of the boundary-layer edge velocity U_{ev}. Also from $\overline{m}$, we can derive the wall and wake boundary-conditions for the EIF calculation. Solving the Euler equations with these boundary-conditions for the outer EIF, we have an inviscid version of boundary-layer edge velocity U_{ei}. Then we can use Carter's relaxation scheme[31] to get an updated guess of the boundary-layer thickness:

$$\frac{\delta^*_{new}}{\delta^*_{old}} = 1 + \omega(\frac{U_{ev}}{U_{ei}} - 1) \tag{25}$$

Here, ω is an under-relaxation factor. Convergence is judged from the difference between the two boundary-layer edge velocities U_{ev} and U_{ei} . Two orders-of-magnitude drop of the difference between these two velocities over the inviscid one is enough for most of cases.

As we solve the Euler equations for the outer EIF, we need four boundary-conditions from the matching requirements of the EIF with the viscous flow for a 2D problem. However, as Sockol and Johnston[32] proved, if we use the surface normal blowing velocity derived from the continuity equation as a boundary condition, then other matching requirements such as the normal flux of streamwise momentum and total enthalpy will automatically be satisfied. Considering a first-order boundary-layer approximation, we can simply calculate the surface values of density, streamwise velocity and total enthalpy via linear extrapolation from the adjacent grid to the wall. Therefore the only change in solving the EIF is that we need to add a blowing velocity in the normal velocity boundary condition on the airfoil surface as in Eqn. (10) if we solve the EIF using Cartesian Euler method. The blowing velocity can be obtained from mass conservation:

$$V_n = \frac{1}{\rho_e}\frac{d}{ds}(\rho U_e \delta^*) = \frac{1}{\rho_e}\frac{d}{ds}(\overline{m}) \tag{26}$$

It is known that the Kutta condition is automatically satisfied in Euler calculations. So in the wake, unlike the boundary-layer coupling with a potential code, we do not need to use a jump condition. We simply treat the wake as two boundary-layers developed on both sides of the dividing streamline of the wake. Currently we assume this dividing streamline is the extension of the airfoil mean chord rather than calculating it accurately.

D. $k-\omega$ Turbulence Model

The code PARCAE developed in our LAB is a 3-D unsteady RANS solver with several turbulence models implemented. In this paper, we use the RANS solver with $k-\omega$ turbulence model for flutter prediction.

The integral form of RANS equations is just the integral form of Euler equations (1) with the viscous fluxes added. For 2-D problems, the viscous fluxes are:

$$\mathbf{G_v} = \begin{bmatrix} 0 \\ \bar{\tau} \cdot \mathbf{e}_x \\ \bar{\tau} \cdot \mathbf{e}_y \\ \bar{\tau} \cdot \mathbf{q} + \mathbf{B} - \mathbf{Q} \end{bmatrix} \tag{27}$$

where

$$\begin{aligned} \mathbf{q} &= u\mathbf{e}_x + v\mathbf{e}_y \\ \bar{\tau} &= \bar{\tau}_{xx}\mathbf{e}_x\mathbf{e}_x + \bar{\tau}_{xy}\mathbf{e}_x\mathbf{e}_y + \bar{\tau}_{yx}\mathbf{e}_y\mathbf{e}_x + \bar{\tau}_{yy}\mathbf{e}_y\mathbf{e}_y \\ \bar{\tau}_{xx} &= \lambda\left(\frac{\partial u}{\partial x} + \frac{\partial v}{\partial y}\right) + 2\mu\frac{\partial u}{\partial x} \\ \bar{\tau}_{xy} &= \bar{\tau}_{yx} = \mu\left(\frac{\partial u}{\partial y} + \frac{\partial v}{\partial x}\right) \\ \bar{\tau}_{yy} &= \lambda\left(\frac{\partial u}{\partial x} + \frac{\partial v}{\partial y}\right) + 2\mu\frac{\partial v}{\partial y} \\ \lambda &= -\frac{2}{3}\mu \\ \mathbf{Q} &= \kappa\nabla T \end{aligned} \tag{28}$$

and thus the integral form of RANS equations can be written as:

$$\frac{\partial}{\partial t}\int_V \mathbf{W}dV + \int_S \mathbf{G}\cdot\mathbf{n}dS - \int_S \mathbf{G}\mathbf{v}\cdot\mathbf{n}dS = 0 \tag{29}$$

The effect of turbulence is accounted for by using the eddy-viscosity hypothesis. That is:

$$\begin{aligned} \mu &= \mu_l + \mu_t \\ \kappa &= \frac{\mu_l}{Pr_l} + \frac{\mu_t}{Pr_t} \\ \mathbf{B} &= (\mu_l + \sigma^*\mu_t)\nabla k \end{aligned} \tag{30}$$

where Pr_l and Pr_t are the laminar and turbulent Prandtl numbers, respectively, the molecular viscosity coefficient μ_l can be obtained by Sutherland's law and the eddy-viscosity μ_t by solving $k-\omega$ turbulent model equations.

The $k-\omega$ turbulence model equations are :

$$\begin{cases} \frac{\partial}{\partial t}(\rho k) + \nabla\cdot(\rho k\mathbf{q}) = \tau : \nabla\mathbf{q} - \beta^*\rho\omega\mathbf{k} + \nabla\cdot[(\mu_\mathbf{l} + \sigma^*\mu_\mathbf{t})\nabla\mathbf{k}] \\ \frac{\partial}{\partial t}(\rho\omega) + \nabla\cdot(\rho\omega\mathbf{q}) = (\alpha\omega/\mathbf{k})\tau : \nabla\mathbf{q} - \beta\rho\omega^\mathbf{2} + \nabla\cdot[(\mu_\mathbf{l} + \sigma\mu_\mathbf{t})\nabla\omega] \end{cases} \tag{31}$$

where k is the turbulent mixing energy, ω is the specific dissipation rate, and

$$\begin{aligned} \mu_t &= \alpha^*\frac{\rho k}{\omega} \\ \tau_{xx} &= 2\mu_t\left[\frac{\partial u}{\partial x} - \frac{1}{3}(\frac{\partial u}{\partial x} + \frac{\partial v}{\partial y})\right] - \frac{2}{3}\rho k \\ \tau_{xy} &= \tau_{yx} = \mu_t\left(\frac{\partial u}{\partial y} + \frac{\partial v}{\partial x}\right) \\ \tau_{yy} &= 2\mu_t\left[\frac{\partial v}{\partial y} - \frac{1}{3}(\frac{\partial u}{\partial x} + \frac{\partial v}{\partial y})\right] - \frac{2}{3}\rho k \end{aligned} \tag{32}$$

The closure coefficients are:

$$\begin{aligned} \beta &= \frac{3}{40};\ \beta^* = \frac{9}{100} \\ \alpha &= \frac{5}{9};\ \ \alpha^* = 1 \\ \sigma &= \frac{1}{2};\ \ \sigma^* = \frac{1}{2} \end{aligned} \tag{33}$$

The $k-\omega$ turbulence model equations (31) can also be solved by Jameson's dual-time stepping scheme and thus strongly coupled with the RANS equations (29). All those convergence acceleration techniques such as local time stepping, residual smoothing, and multigrid can be applied. The readers are referred to Ref. 23 for more details.

E. Structural Solver

We use modal analysis to solve for the structural deformation under aerodynamic forcing. For each mode i, the modal equations are:

$$\ddot{\eta}_i + 2\zeta_i\omega_i\dot{\eta}_i + \omega_i^2\eta_i = Q_i \tag{34}$$

where η_i is the generalized normal mode displacement, ζ_i is the modal damping, ω_i is the decoupled modal frequency, and Q_i is the generalized aerodynamic force.

The structural displacement vector can be written as the sum of all the modal shapes:

$$\{q\} = \sum_{i=1}^{N} \eta_i\{\phi_i\} \tag{35}$$

where $\{\phi_i\}$ is the modal shape of the i-th mode.

Equation (34) can be converted into a first-order system of equations and integrated in time by a second-order fully implicit scheme. Following Alonso and Jameson,[33] we assume:

$$x_{1i} = \eta_i, \qquad x_{2i} = \dot{x}_{1i} \tag{36}$$

for each of the modal equations. We can then rewrite Eq. (34) in Matrix form as

$$\{\dot{X}_i\} = [A_i]\{X_i\} + \{F_i\}, \qquad i = 1, N \tag{37}$$

where

$$\{\dot{X}_i\} = \begin{Bmatrix} x_{1i} \\ x_{2i} \end{Bmatrix}, \quad [A] = \begin{bmatrix} 0 & 1 \\ -\omega_i^2 & -2\omega_i\zeta_i \end{bmatrix}, \quad \{F_i\} = \begin{Bmatrix} 0 \\ Q_i \end{Bmatrix} \tag{38}$$

Equation (37) can be decoupled to be

$$\begin{cases} \frac{dz_{1i}}{dt} = \omega_i(-\zeta_i + \sqrt{\zeta_i^2 - 1})z_{1i} + \frac{(-\zeta_i + \sqrt{\zeta_i^2 - 1})}{2\sqrt{\zeta_i^2 - 1}}Q_i \\ \frac{dz_{1i}}{dt} = \omega_i(-\zeta_i + \sqrt{\zeta_i^2 - 1})z_{1i} + \frac{(-\zeta_i + \sqrt{\zeta_i^2 - 1})}{2\sqrt{\zeta_i^2 - 1}}Q_i \end{cases} \tag{39}$$

where

$$\{Z_i\} = \begin{Bmatrix} z_{1i} \\ z_{2i} \end{Bmatrix} = P^{-1}\{X_i\} \tag{40}$$

and P_i is the diagonalization matrix:

$$P_i = \begin{bmatrix} (-\zeta_i - \sqrt{\zeta_i^2 - 1})/\omega_i & (-\zeta_i + \sqrt{\zeta_i^2 - 1})/\omega_i \\ 1 & 1 \end{bmatrix} \tag{41}$$

We use the same second-order-accurate fully implicit scheme as Eq. (7) to integrate the preceding equations in time:

$$\begin{cases} \frac{3z_{1i}^{n+1} - 4z_{1i}^{n} + z_{1i}^{n-1}}{2\Delta t} = -R_{1i}(z_{1i}^{n+1}, Q_i^{n+1}) = \omega_i(-\zeta_i + \sqrt{\zeta_i^2 - 1})z_{1i}^{n+1} + \frac{(-\zeta_i + \sqrt{\zeta_i^2 - 1})}{2\sqrt{\zeta_i^2 - 1}}{Q_i}^{n+1} \\ \frac{3z_{2i}^{n+1} - 4z_{2i}^{n} + z_{2i}^{n-1}}{2\Delta t} = -R_{2i}(z_{2i}^{n+1}, Q_i^{n+1}) = \omega_i(-\zeta_i - \sqrt{\zeta_i^2 - 1})z_{2i}^{n+1} + \frac{(\zeta_i + \sqrt{\zeta_i^2 - 1})}{2\sqrt{\zeta_i^2 - 1}}{Q_i}^{n+1} \end{cases} \tag{42}$$

Also we can reformulate the above equation into a pseudotime format as Eqs. (8) and (9):

$$\begin{cases} \frac{dz_{1i}}{dt^*} + {R_{1i}}^*(z_{1i}, Q_i) = 0 \\ \frac{dz_{2i}}{dt^*} + {R_{2i}}^*(z_{2i}, Q_i) = 0 \end{cases} \tag{43}$$

where

$$\begin{cases} {R_{1i}}^*(z_{1i}, Q_i) = \frac{3z_{1i} - 4z_{1i}^n + z_{1i}^{n-1}}{2\Delta t} + R_{1i}(z_{1i}, Q_i) \\ {R_{2i}}^*(z_{2i}, Q_i) = \frac{3z_{2i} - 4z_{2i}^n + z_{2i}^{n-1}}{2\Delta t} + R_{2i}(z_{2i}, Q_i) \end{cases} \tag{44}$$

The deformation of the wing, represented by z_{1i} and z_{2i} , influences the flow field and, thus the aerodynamic force Q_i. Conversely, the aerodynamic force Q_i determines the deformation of the wing. Therefore, the structural equations must be solved together with the flow equations simultaneously. If we use Euler equations for the flow solver, Eqs. (8) and (43) can be regarded as one single system of time-dependent equations in the pseudotime t^*, which can be solved by the efficient explicit time-marching methods until a steady state is reached. Once the computation reaches a steady state in the pseudotime t^*, the solutions to Eqs. (8) and (43) become the time-accurate solution of the implicit fully coupled CFD-CSD equations (7) and (42) in one physical time step without any time lag between the CFD and CSD solvers. This method was used for wing flutter calculation in Ref. 4.

III. Results and Discussions

We use the five methods in a coupled CFD-CSD approach for the 2-D Isogai wing model,[19,20] Case A. This model simulates the bending and torsional motion of a wing cross-section in the outboard portion of a swept wing. It consists of two degrees of freedom, plunging and pitching, for a NACA 64A010 airfoil. The length scale is nondimensionalized by half chord b and the time by $\frac{1}{\omega_\alpha}$. The nondimensional structure parameters thus are: $r_\alpha^2 = 3.48$, $x_\alpha = 1.8$, $a = -2.0$, $\mu = 60$ and the ratio of uncoupled natural frequencies $\frac{\omega_h}{\omega_\alpha} = 1.0$. For this two-degree-of-freedom structure, there are only two modes, and the wind-off natural frequencies are 0.71377 and 5.337 with corresponding modal shapes $(1.0, 0.536)^t$ and $(1.0, -0.536)^t$, respectively. We can see the first mode is a symmetrical one while the second is antisymmetric. So the response of the system under aerodynamic forces will be a combination of these two modes and there may be a phase difference between the plunging and pitching displacements.

A. Inviscid Flow Results

Methods (1) and (2) are for inviscid flow calculation. Both methods employ the Euler equations but on different grids. The grid used in method (1) is a 128×48 non-moving Cartesian grid with 80 nodes on either side of the airfoil, while method (2) uses a 192×32 moving C grid with 128 nodes on the airfoil surface. In this subsection, we compare the results of flutter prediction by these two methods.

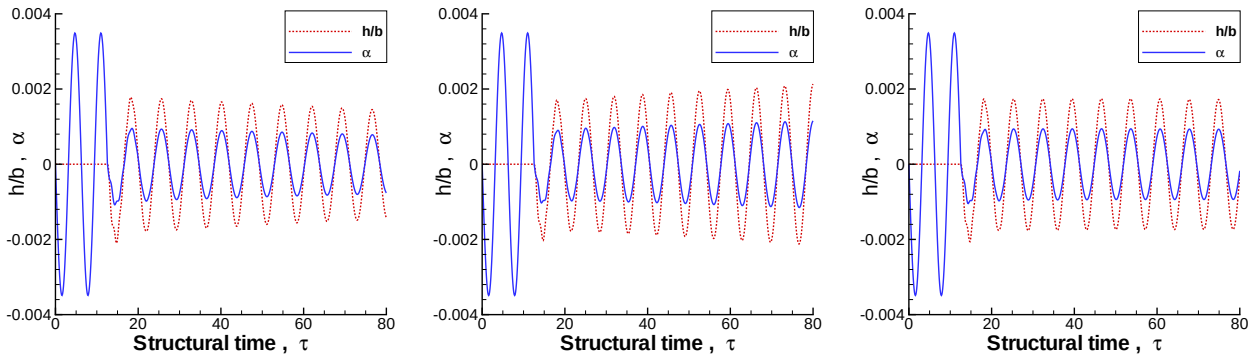

(a) $V^* = 0.62$, stable situation. (b) $V^* = 0.72$, unstable situation. (c) $V^* = 0.67$, neutral situation.

Figure 1. Time histories of the pitching and plunging amplitudes for $M_\infty = 0.825$.

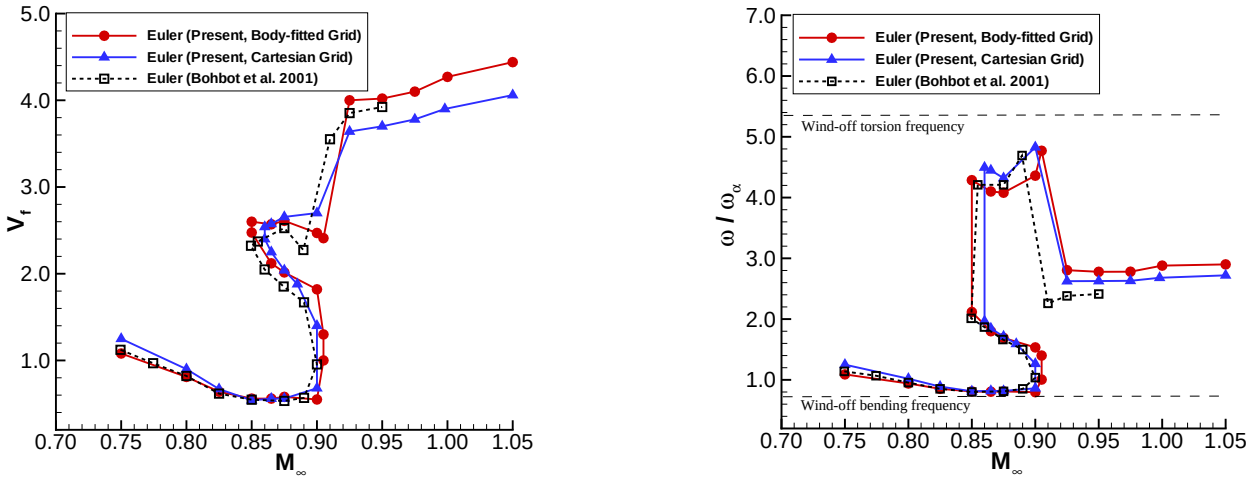

Figure 2. Inviscid flutter boundary.

For flutter calculation, two cycles of forced pitching are performed first and then the airfoil is free to move by itself. Figure 1 shows the flutter computational results for the Isogai wing model at a flight Mach number of 0.825 using method (1). Plotted in the figure are the time histories of the pitching and plunging amplitudes. The speed index V^* is defined as

$$V^* = \frac{U_\infty}{b\omega_\alpha\sqrt{\mu}} \tag{45}$$

For $V^* = 0.62$, both of the pitching and plunging amplitudes decay with time, indicating that the aeroelastic system is stable for this particular condition. At a higher V^*, the system may become less and less stable until one or both of the pitching and plunging motions diverge when $V^* = 0.72$. In between these two V^* conditions, there is a particular point where the system is neutrally stable. The figure shows this happens when $V^* = 0.67$. The speed index at the neutral condition is called flutter speed index or flutter boundary and denoted by V_f.

A converging point and a diverging point like the above are first identified, from which we can interpolate the V^* in between to obtain an estimate of the neutral point. We then perform a computation with the new V^* to see if it is above or below the stability limit, or perhaps right at the neutral point. It may take several runs for a given free-stream Mach number before the V^* corresponding to the neutral stability point,or say V_f, can be accurately located by this "bi-section" method. In this way, computations for a number of free-stream Mach numbers for the Isogai wing model are performed using both methods (1) and (2) and the results are compared in Fig. 2 together with the Euler result by Bohbot et al.[34]

All three Euler results show an S-shaped flutter boundary and agree with each other well. All predict the transonic dip at about $M = 0.85$, and the flutter boundaries bend back at around $M = 0.90$ resulting in a small range of Mach numbers in the transonic region with multiple flutter boundaries. This range predicted by the Cartesian Euler method covers the Mach number from 0.865 to 0.900 and is a little narrower than those predicted by the other two body-fitted methods. In addition, the Cartesian Euler method predicts the flutter boundary somewhat higher in the low Mach number region while lower in the high transonic and supersonic region.

For low Mach numbers until the bend-back point, the flutter frequencies are close to the first coupled wind-off frequency indicating that the flutter is primarily of the first mode. However, the flutter frequencies of those third flutter boundary points in the multiple flutter boundary region are close to the second coupled wind-off frequency indicating those points are primarily the second mode flutter. Flutter frequencies for other flutter points are in between the two coupled wind-off frequencies, 0.71377 and 5.337. For any Mach number with multiple flutter boundaries, the first flutter point (with low V^*) is primarily the first mode flutter and the third point mainly of the second mode. This can be clearly seen from Fig. 3 which shows the time histories of the structural displacements as well as mode amplitudes for three flutter points of Mach number 0.875 obtained by method (2). As we mentioned earlier that the first mode is symmetrical and the

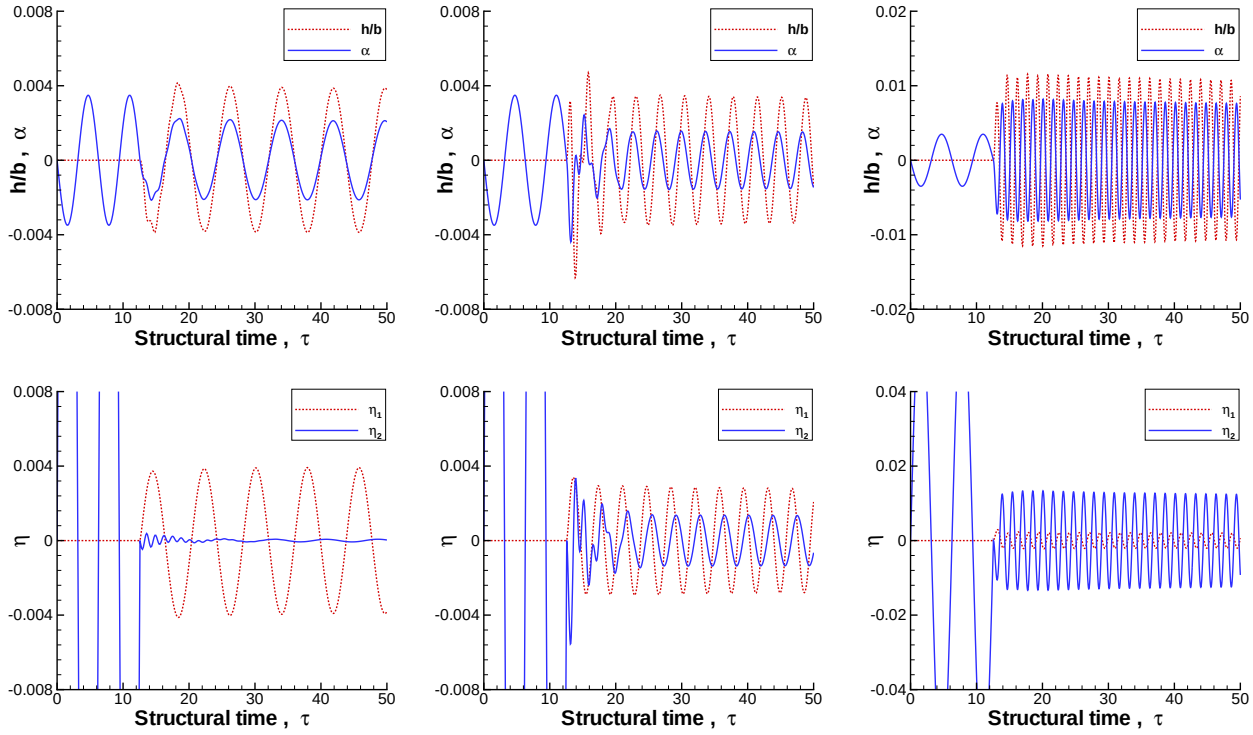

(a) First flutter point, $V_f = 0.56$ (b) Second flutter point, $V_f = 2.01$ (c) Third flutter point, $V_f = 2.61$

Figure 3. Time histories of the structural displacements and mode amplitudes for $M_\infty = 0.875$.

second mode antisymmetric, it is no wonder that the pitching and plunging displacements are roughly in phase for the first flutter point while there is obvious phase difference for the second flutter point and the phase lag is almost equal to π for the third flutter point.

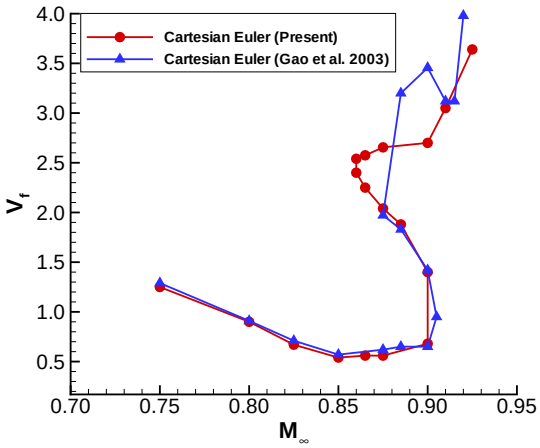

Figure 4. Comparison of flutter boundary.

Gao et al.[16] predicted the flutter boundary for the Isogai wind model using method (1) earlier and their result is compared with our current result in Fig. 4. The two sets of results almost coincide with each other except in the higher V_f portion of the boundary. The discrepancy is due to the fact that Gao et al. used a fixed 32 time steps in one period based on ω_α for all the flutter calculations. This is adequate for the points on the lower portion of the flutter boundary. In the higher V_f portion, Fig. 2 indicates a much higher flutter frequency $\frac{\omega}{\omega_\alpha}$. The original 32 time steps per period based on ω_α become only 8 time steps per period when $\frac{\omega}{\omega_\alpha}$ approaches 4. This lack of time resolution is responsible for the discrepancy between the two solutions. In our current calculation, we use variable numbers of time steps to maintain at least 50 time steps based on the actual $\frac{\omega}{\omega_\alpha}$.

B. Viscous Flow Results

Methods (3) and (4) use the Euler equations coupled with an integral boundary-layer. Method (5) is a Full Navier-Stokes method. The grids used for the Euler solver are the same as those for the inviscid calculations, while the Navier-Stokes solver uses a 176×64 C grid with 128 nodes on the airfoil surface. The Reynolds number of 6.0×10^6 is used for all calculations.

Following the same "bi-section" method described in the last subsection, we can map out the flutter boundary of the Isogai wing model using the three methods and the comparison of the results is shown in

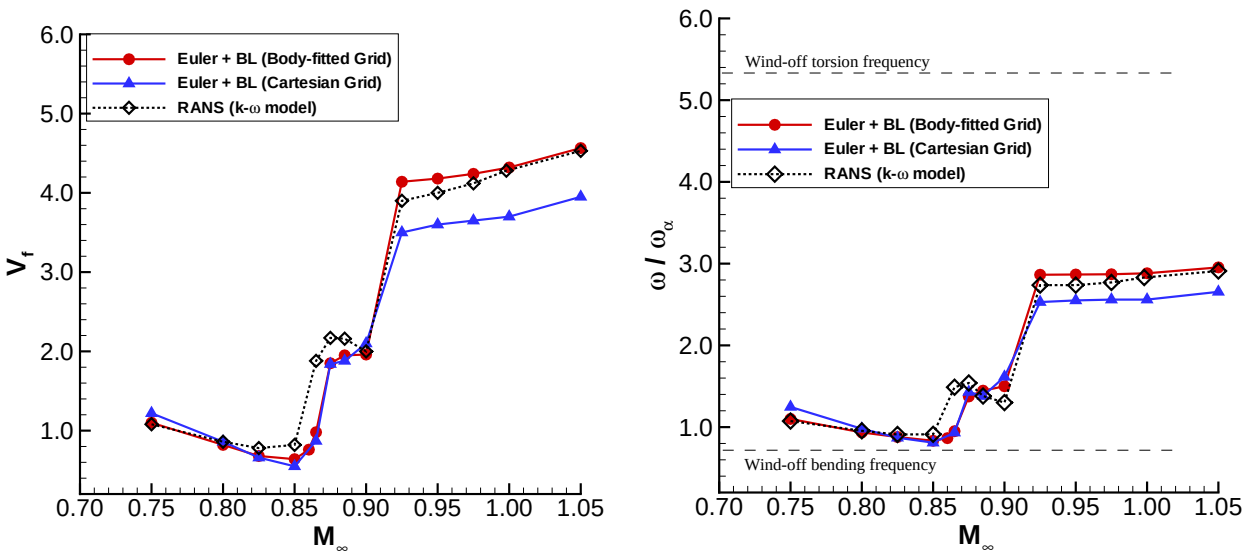

Figure 5. Viscous flutter boundary.

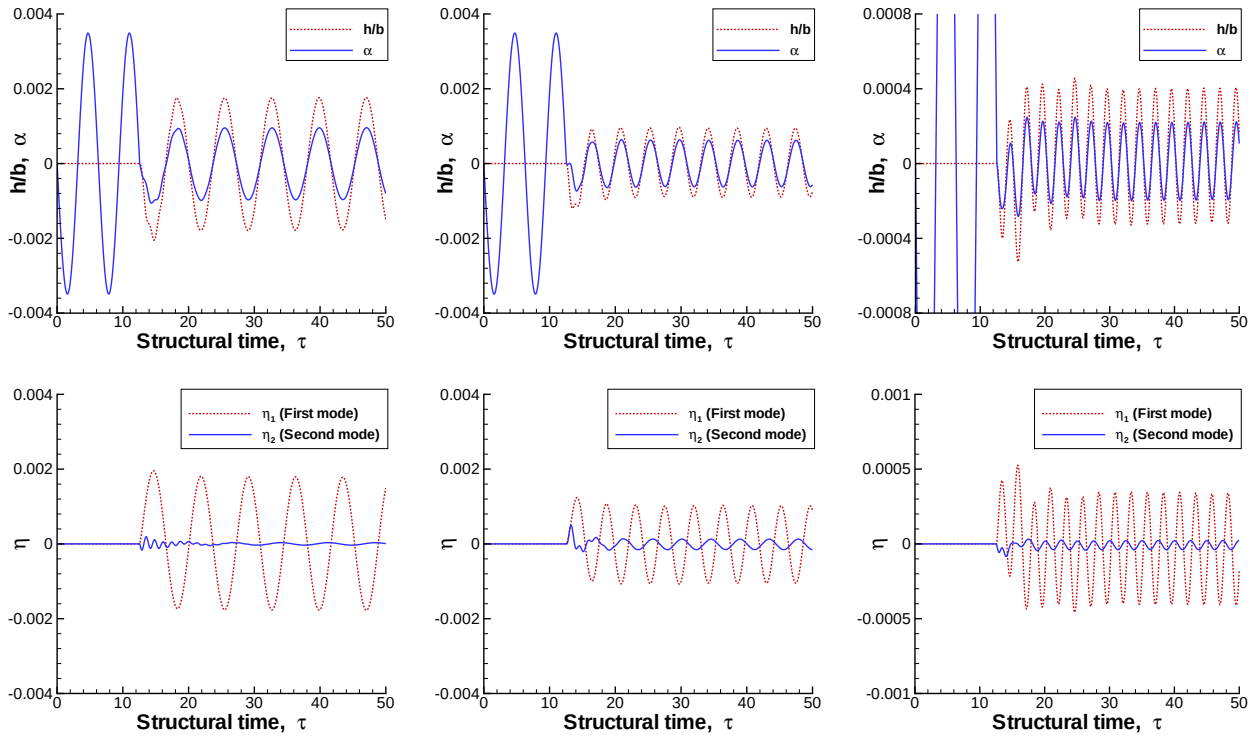

(a) $M = 0.825$, $V_f = 0.66$ (b) $M = 0.875$, $V_f = 1.84$ (c) $M = 0.925$, $V_f = 3.50$

Figure 6. Time histories of the structural displacements and mode amplitudes.

Fig. 5. No multiple flutter boundary region exists for the viscous calculations. All three flutter boundaries follow well with each other. Right after the transonic dip at about Mach number 0.85, there is a sharp increase. In the Mach number range of $0.875 - 0.90$, there is a slight step. The Navier-Stokes result shows a small decrease while the two boundary-layer coupling results continue to increase gradually in that Mach number range. After $M = 0.90$, the flutter boundary increases dramatically again until Mach number 0.925 and then continues to increase slowly into the supersonic region. In the transonic Mach number range $0.80 - 0.90$, the two boundary layer coupling results agree with each other very well, but they are lower than what the Navier-Stokes solver predicts. However, for both lower and higher ends, the result of boundary-layer coupling with the Euler on body-fitted grid method seems to agree with the full Navier-Stokes result well, while the boundary-layer coupling with the Cartesian Euler method tends to predict higher flutter boundary for lower Mach numbers and lower boundary for higher Mach numbers. The flutter frequency curves behave similarly.

Plotted in Fig. 6 are the time histories in flutter of the structural displacements as well as mode amplitudes predicted by method (3) at three Mach numbers. For all three representative Mach numbers, the amplitude of the first mode is much larger than that of the second mode, and thus the plunging and pitching displacements are almost in phase. In fact, the viscous solvers predict primarily first mode flutter for all Mach numbers.

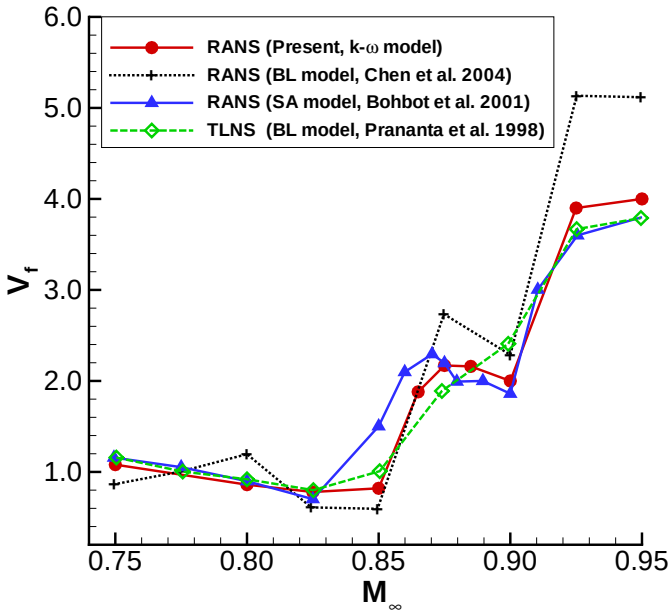

Figure 7. Comparison of flutter boundary by Navier-Stokes solvers.

We compare other three Navier-Stokes results found in literature with ours in Fig. 7. The result by Bohbot et al.[34] is obtained by using the Sparlart-Allmaras turbulence model. Prananta et al.[35] use a thin-layer-Navier-Stokes (TLNS) solver with the Baldwin-Lomax turbulence model. Chen et al.[36] also use the Baldwin-Lomax turbulence model but a full Navier-Stokes solver. Prananta et al. predict an increase other than a decrease of flutter boundary in the Mach number range of $0.875 - 0.90$, probably due to the use of TLNS. Chen et al. predict a much higher flutter-boundary level in the high transonic Mach number range, which may be partially because of the relatively high Reynolds number of 12.56×10^6 used in their calculation. Prananta et al. use the same Reynolds number of 6.0×10^6 as in our calculation, while Bohbot et al. do not fix the Reynolds number. In the Mach number range of $0.825 - 0.875$, Bohbot et al. predict a higher flutter boundary level than the other three results. In the low Mach number region, all results are smooth and agree with each other well except that the result of Chen et al. is somewhat wavy.

In order to see what differences viscosity can make, we compare the flutter boundaries by the Cartesian Euler method with or without boundary-layer correction together with the full Navier-Stokes result in Fig. 8. The major difference is in the transonic Mach number range $0.85 - 0.90$. In that region, the inviscid solver predicts multiple flutter boundaries. However, with viscosity considered either by boundary-layer coupling or by using the full Navier-Stokes equations, the flutter boundary is single-valued. Viscous effects reduce

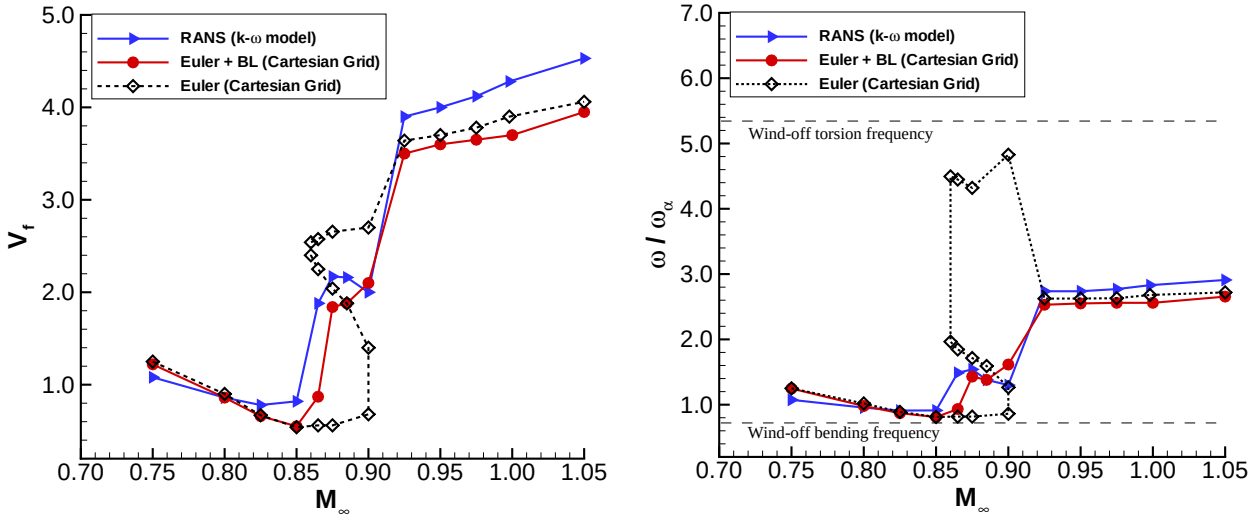

Figure 8. Comparison of inviscid and viscous flutter boundary.

the transonic dip and fills up the bulge of the inviscid flutter boundary. In the low Mach number range and high transonic and supersonic region, the effect of viscosity tends to vanish and thus the flutter boundaries predicted by the inviscid and viscous solvers agree with each other well.

C. Limit Cycle Oscillation

At a speed index V^* beyond the flutter boundary at a given Mach number, the structural displacements may increase sharply from the initial disturbance to a large value and remain constant, reaching the so-called Limit-Cycle Oscillation (LCO) state. LCO is a typical non-linear phenomenon. Since viscosity changes the non-linear property of the flow field at transonic region, LCO may be affected by viscosity significantly.

Plotted in Fig. 9 is the comparison of the LCO frequencies and amplitudes predicted by the Euler on the body-fitted grid method and the full Navier-Stokes solver at three representative Mach numbers: 0.825, 0.875, 0.95.

For low Mach number 0.825, the LCO amplitudes predicted by the Euler solver are several times larger than those by the Navier-Stokes solver. However, at Mach number 0.875, the LCO amplitudes by the Navier-Stokes solver rise sharply with the increase of V^* and are larger than what the Euler solver predicts. At Mach number 0.95, the Euler results again are larger than those by the Navier-Stokes method although the difference is small. The Navier-Stokes LCO frequencies are a little higher than the Euler frequencies for Mach number 0.825 and 0.950. However, for $M = 0.875$, the Euler LCO frequencies are much higher than the Navier-Stokes frequencies due to the second mode LCO predicted by the Euler solver. By looking into the flow fields during LCO, we find out that for $M = 0.825$, the Navier-Stokes LCO flow field has a small separation at the trailing edge and the shockwave moving displacement on the airfoil surface is reduced compared to the Euler LCO. This tells us that viscosity damps the LCO system at low Mach numbers like 0.825 and results in lower LCO amplitudes. However, at Mach number 0.875, the Navier-Stokes LCO has extensive separation on almost the whole airfoil surface and the shockwave is moving from the trailing edge to the leading edge during LCO. That may be the reason why the LCO amplitudes by the Navier-Stokes solver are much larger than the inviscid results for this Mach number. At high transonic Mach number 0.950, both NS and Euler results show the shockwave remains at the trailing edge during LCO and the boundary-layer is attached. Viscosity slightly damps the LCO system for this Mach number.

IV. Conclusions

This paper presents a systematic study of the flutter prediction of the 2-D Isogai wing model using five different methods. The two Euler methods predict an S-shaped flutter boundary, while the two boundary-layer coupling methods as well as the full Navier-Stokes method predict single flutter boundary for the

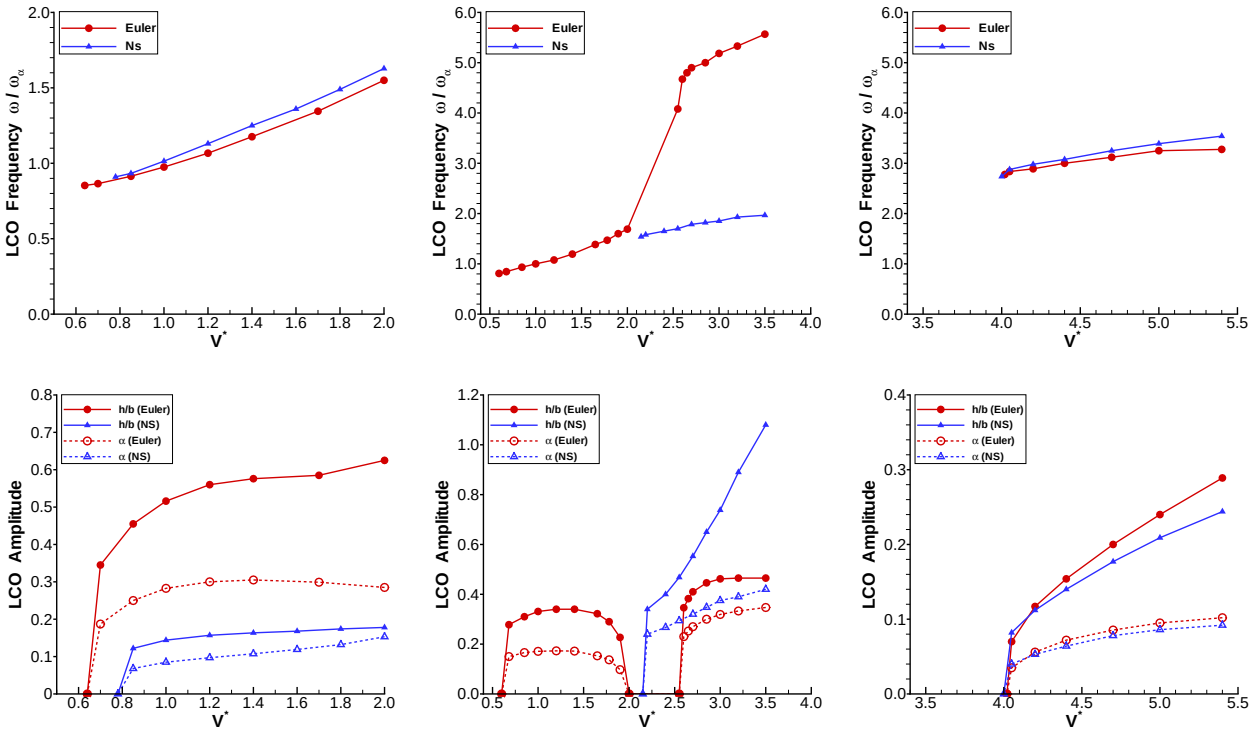

(a) $M = 0.825$ (b) $M = 0.875$ (c) $M = 0.950$

Figure 9. Comparison of LCO frequencies and amplitudes.

whole Mach number range considered. The two inviscid methods show second mode flutter for those third flutter boundary points in the multiple flutter boundary region, but the other three viscous results show only first mode flutter. The comparison of the results obtained shows that the Cartesian Euler method gives comparable flutter prediction as the Euler method using full boundary conditions on body-fitted grids, and also the boundary-layer coupling with the Euler methods provide reasonably good results compared to the full Navier-Stokes solver. The predictions of LCO amplitudes show that viscosity generally damps the system and reduces the amplitudes. However, when extensive separation occurs, the interaction of the shock wave with the separated boundary-layer results in larger LCO amplitudes compared to inviscid predictions.

Appendix

For the Runge-Kutta integration of the four ordinary differential equations in the inverse boundary-layer calculation, we need correlations for those parameters in the equations. We follow the correlations presented in Green's paper:[28]

$$Re_\theta = \frac{\rho_e U_e \theta}{\mu_e}$$

$$F_c = (1 + \frac{\gamma - 1}{2} M_e^2)^{0.5}, \;\; F_R = 1 + 0.056 M_e^2$$

$$C_{f0} = (\frac{0.01013}{log_{10}(F_R Re_\theta) - 1.02} - 0.00075)/F_c$$

$$\frac{\overline{H}}{\overline{H}_0} = \overline{H} \left\{ 1 - 6.55 \left[\frac{C_{f0}}{2} (1 + 0.04 M_e^2) \right]^{0.5} \right\}$$

$$C_f = C_{f0} \left\{ 0.9 (\frac{\overline{H}}{\overline{H}_0} - 0.4)^{-1} - 0.5 \right\}$$

$$H = (\overline{H}+1)\left(1+\frac{\gamma-1}{2}rM_e^2\right)-1$$

$$H_1 = 3.15 + \frac{1.72}{\overline{H}-1} - 0.01(\overline{H}-1)^2$$

$$\overline{F} = \frac{0.02C_E + C_E^2 + 0.8C_{f0}/3}{0.01+C_E}$$

$$C_\tau = (0.024C_E + 1.2C_E^2 + 0.32C_{f0})(1+0.1M_e^2)$$

$$\left(\frac{\theta}{U_e}\frac{dU_e}{dx}\right)_{EQ0} = \frac{1.25}{H}\left[\frac{C_f}{2} - \left(\frac{\overline{H}-1}{6.432\overline{H}}\right)^2 (1+0.04M_e^2)^{-1}\right]$$

$$(C_E)_{EQ0} = H_1\left[\frac{C_f}{2} - (H+1)\left(\frac{\theta}{U_e}\frac{dU_e}{dx}\right)_{EQ0}\right]$$

$$(C_\tau)_{EQ0} = (0.024(C_E)_{EQ0} + 1.2(C_E)_{EQ0}^2 + 0.32C_{f0})(1+0.1M_e^2)$$

$$C = (C_\tau)_{EQ0}(1+0.1M_e^2)^{-1}\lambda^{-2} - 0.32C_{f0}$$

$$(C_E)_{EQ} = (C/1.2 + 0.0001)^{0.5} - 0.01$$

$$\left(\frac{\theta}{U_e}\frac{dU_e}{dx}\right)_{EQ} = \left[\frac{C_f}{2} - \frac{(C_E)_{EQ}}{H_1}\right]/(H+1)$$

Here, λ is a parameter to account for secondary influences such as wall curvature. Currently we ignore those secondary influences and thus set $\lambda = 1$ on the airfoil wall . However in the wake, we set $\lambda = 0.5$ as well as $C_f = C_{f0} = 0$ as suggested by Green.[28]

Acknowledgement

This work is partially supported by NASA Langley Research Center, contract number NAG-1-02050. The authors also thank Drs. John Edwards and Robert Bartels of NASA Langley for many fruitful discussions and information on the integral boundary-layer method.

References

[1]Rodden, W. P. and Johnson, E. H., *MSC/NASTRAN Aeroelastic Analysis User's Guide, Version 68*, The Macneal-Schwender Corporation, Los Angeles, 1994.

[2]Lee-Rausch, E. M. and Batina, J. T., "Wing Flutter Boundary Prediction Using Unsteady Euler Aerodynamic Method," *Journal of Aircraft*, Vol. 32, No. 2, Mar.-Apr. 1995, pp. 416–422.

[3]Lee-Rausch, E. M. and Batina, J. T., "Wing Flutter Computations Using an Aerodynamic Model Based on the Navier-Stokes Equations," *Journal of Aircraft*, Vol. 33, No. 6, Nov.-Dec. 1996, pp. 1139–1147.

[4]Liu, F., Cai, J., Zhu, Y., Wong, A. S. F., and Tsai, H.-M., "Calculation of Wing Flutter by a Coupled Fluid-Structure Method," *Journal of Aircraft*, Vol. 38, No. 2, Mar.-Apr. 2001, pp. 334–342.

[5]Gibbons, M., "Aeroelastice Calculations Using CFD for a Typical Business Jet Model," NASA CR 4753, 1996.

[6]Bartels, R., "Flow and Turbulence Modeling and Computation of Shock Buffet Onset for Conventional and Supercritical Airfoils," NASA TP 1998-206908, 1998.

[7]Tang, L., Bartels, R., Chen, P., and Liu, D. D., "Numerical Investigation of Transonic Limit Oscillations of a 2-D supercritical Wing," AIAA Paper 2001-1290, 2001.

[8]Batina, J. T., "A Finite-Difference Approximate-Factorization Algorithm for Solution of the Unsteady Transonic Small-Disturbance Equation," NASA TP 3129, Jan. 1992.

[9]Edwards, J., "Transonic Shock Oscillations Calculated with a New Interactive Boundary Layer Coupling Method," AIAA Paper 93-0777, 1993.

[10]Edwards, J., "Transonic Shock Oscillations and Wing Flutter Calculated with an Interactive Boundary Layer Coupling Method," *EUROMECH-Colloquium 349, Simulation of Fluid-Structure Interaction in Aeronautics*, Gottingen, Germany, Sept. 1996.

[11]Whitfield, D., Swafford, T., and Jacocks, J., "Calculation of Turbulent Boundary Layers with Separation and Viscous-Inviscid Interaction," *AIAA Journal*, Vol. 19, No. 10, 1981, pp. 1315–1322.

[12]Lee, T. J., *Transonic Viscous-Inviscid Interaction Using Euler and Inverse Boundary-Layer Equations*, Ph.D. dissertation, Mississippi State Univ., Dec. 1983.

[13]Giles, M., Drela, M., and Thompkins, W. T., "Newton Solution of Direct and Inverse Transonic Euler Equations," AIAA Paper 85–1530, AIAA 7th Computational Fluid Dynamics Conference, Cincinnati, Ohio, June 1985.

[14]Beaumiera, P., Arnaudb, G., and Castellinb, C., "Performance prediction and flow field analysis of rotors inhover using a coupled Euler/boundary layer method," *Aerosp.Sci.Technol*, , No. 3, 1999, pp. 473–484.

[15]Gao, C., Luo, S., and Liu, F., "Calculation of Unsteady Transonic Flow by an Euler Method with Small Perturbation Boundary Conditions," AIAA Paper 2003-1267, Jan. 2003.

[16]Gao, C., Luo, S., Liu, F., and Schuster, D. M., "Calculation of Airfoil Flutter by an Euler Method with Approximate Boundary Conditions," AIAA Paper 2003-3830, June 2003.

[17]Schuster, D. M., Liu, D. D., and Huttsell, L. J., "Computational Aeroelasticity: Success, Progress, Challenge," *Journal of Aircraft*, Vol. 40, No. 5, 2003, pp. 843–856.

[18]Dowell, E., Edwards, J., and Strganac, T., "Nonlinear Aeroelasticity," *Journal of Aircraft*, Vol. 40, No. 5, 2003, pp. 857–874.

[19]Isogai, K., "On the Transonic-Dip Mechanism of flutter of a Sweptback Wing," *AIAA Journal*, Vol. 17, No. 7, July 1979, pp. 793–795.

[20]Isogai, K., "On the Transonic-Dip Mechanism of flutter of a Sweptback Wing: Part II," *AIAA Journal*, Vol. 19, No. 9, Sept. 1981, pp. 1240–1242.

[21]Zhang, Z., Liu, F., and Schuster, D. M., "Calculation of Unsteady Flow and Flutter by an Euler and Integral Boundary-Layer Method on Cartesian Grids," AIAA Paper 2004-5203, Aug. 2004.

[22]Yang, S., Zhang, Z., Liu, F., and Schuster, D. M., "Time-Domain Aeroelastic Simulations with Small Perturbation Boundary Conditions and Integral Boundary-Layer Method," AIAA Paper 2004-5377, Aug. 2004.

[23]Liu, F. and Zheng, X., "A Strongly-Coupled Time-Marching Method for Solving the Navier-Stokes and k-ω Turbulence Model Equations with Multigrid," *J. of Computational Physics*, Vol. 128, 1996.

[24]Jameson, A., "Time dependent calculations using multigrid, with applications to unsteady flows past airfoils and wings," AIAA Paper 91–1596, June 1991, 10th AIAA Computational Fluid Dynamics Conference.

[25]Jameson, A., Schmidt, W., and Turkel, E., "Numerical Solutions of the Euler Equations by Finite Volume Methods Using Runge-Kutta Time-Stepping Schemes," AIAA Paper 81–1259, June 1981.

[26]Vatsa, V. and Carter, J., "Development of an Integral Boundary-Layer Technique for Separated Turbulent Flow," United Technologies Research Center Report UTRC81-28, 1981.

[27]Head, M., "Entrainment in the turbulent boundary layer," A.R.C.R.&M. 3152, 1958.

[28]Green, J. E., Weeks, D. J., and Brooman, J. W. F., "Prediction of Turbulent Boundary Layers and Wakes in Compressible Flow by a Lag-Entrainment Method," British Aeronautical Research Council R & M 3791, 1977.

[29]Thwaites, B., "Approximate Calculation of the Laminar Boundary Layer," *Aeronaut. Q.*, Vol. 1, No. 6, 1949, pp. 245–280.

[30]Michel, R., "Etude de la Transition sur les Profiles d'Aile," ONERA Report 1/1578A, 1951.

[31]Carter, J. E., "A New Boundary-Layer Inviscid Iteration Technique for Separated Flow," AIAA Paper 1979-1450, 1979.

[32]Sockol, P. M. and Johnston, W. A., "Coupling Conditions for Integrating Boundary Layer and Rotational Inviscid Flow," *AIAA Journal*, Vol. 24, No. 6, June 1986, pp. 1033–1035.

[33]Alonso, J. J. and Jameson, A., "Fully-Implicit Time-Marching Aeroelastic Solutions," AIAA Paper 94–0056, Jan. 1994.

[34]Julien Bohbot, D. D., "Time Domain Analysis of Two D.O.F. Airfoil Flutter Using an Euler/Turbulent Navier-Stokes Implicit Solver," *International Forum on Aeroelasticity and Structural Dynamics*, Madrid, Spain, 2001.

[35]Prananta, B. B., L., H. M. H., and J., Z. R., "Two-Dimensional Transonic Aeroelastic Analysis Using Thin-Layer Navier-Stokes Method," *Journal of Fluid and Structures*, Vol. 12, 1998, pp. 655–676.

[36]Xiangying Chen, G.-C. Z. and Hu, Z., "Flutter Prediction Based on Fully Coupled Fluid-Structural Interactions," 9th national turbine engine high cycle fatigue conference, 2004.